

## Superfluid helium ultralight dark matter detector

M. Hirschel<sup>1</sup>, V. Vadakkumbatt<sup>1</sup>, N. P. Baker<sup>1</sup>, F. M. Schweizer<sup>1</sup>, J. C. Sankey<sup>2</sup>, S. Singh,<sup>3</sup> and J. P. Davis<sup>1</sup>

<sup>1</sup>*Department of Physics, University of Alberta, Edmonton, Alberta T6G 2E9, Canada*

<sup>2</sup>*Department of Physics, McGill University, Montréal, Québec H3A 2T8, Canada*

<sup>3</sup>*Department of Electrical and Computer Engineering, University of Delaware, Newark, Delaware 19716, USA*



(Received 2 September 2023; accepted 9 April 2024; published 10 May 2024)

The absence of a breakthrough in directly observing dark matter (DM) through prominent large-scale detectors motivates the development of novel tabletop experiments probing more exotic regions of the parameter space. If DM contains ultralight bosonic particles, they would behave as a classical wave and could manifest through an oscillating force on baryonic matter that is coherent over  $\sim 10^6$  periods. Our Helium ultraLight dark matter Optomechanical Sensor (HeLIOS) uses the high- $Q$  acoustic modes of superfluid helium-4 to resonantly amplify this signal. A superconducting reentrant microwave cavity enables sensitive optomechanical readout ultimately limited by thermal motion at millikelvin temperatures. Pressurizing the helium allows for the unique possibility of tuning the mechanical frequency to effectively broaden the DM detection bandwidth. We demonstrate the working principle of our prototype HeLIOS detector and show that future generations of HeLIOS could explore unconstrained parameter space for both scalar and vector ultralight DM after just an hour of integration time.

DOI: [10.1103/PhysRevD.109.095011](https://doi.org/10.1103/PhysRevD.109.095011)

### I. INTRODUCTION

While numerous astrophysical observations support the existence of dark matter (DM) [1–3], its first direct detection is still awaited and is one of the greatest ambitions in modern science. Tremendous efforts toward detecting popular DM candidates like weakly interacting massive particles have not been successful yet, motivating a stronger focus on more exotic regions of the DM parameter space, with a possible mass range spanning approximately 90 orders of magnitude [4,5]. Extending the search into these territories is accompanied by the need for novel detection paradigms, with a growing focus on small-scale quantum systems as precise detectors for lowest-mass DM candidates [6,7].

Ultralight dark matter (UDM) denotes particle candidates with masses  $m_{\text{dm}} < 10 \text{ eV}/c^2$  [8,9]. In this range, the local DM density  $\rho_{\text{dm}} = 0.4 \text{ GeV}/\text{cm}^3$  implies a bosonic particle occupation exceeding 1 in each de Broglie volume  $\lambda_{\text{dB}}^3$ , with  $\lambda_{\text{dB}} = h/m_{\text{dm}}v_{\text{vir}}$  and particle velocity  $v_{\text{vir}} \approx 10^{-3}c$  in the virialized DM halo [10]. As a result, UDM particles would behave wavelike, i.e., could either be described through a classical (pseudo)scalar field  $\Phi(\mathbf{x}, t) \approx \Phi_0 \cos(\omega_{\text{dm}}t - \mathbf{k}_{\text{dm}} \cdot \mathbf{x})$  (for spin  $S = 0$ ), or vector field  $A_\mu(\mathbf{x}, t) \approx A_{\mu,0} \cos(\omega_{\text{dm}}t - \mathbf{k}_{\text{dm}} \cdot \mathbf{x})$  (for  $S = 1$ ), oscillating at the Compton frequency  $\omega_{\text{dm}} = m_{\text{dm}}c^2/\hbar$  with wave vector  $|\mathbf{k}_{\text{dm}}| = 2\pi/\lambda_{\text{dB}}$  [10–13]. Significant efforts toward UDM detection have been devoted to axions [14]—pseudoscalar particles in the  $\mu\text{eV}$ -range—for

example through haloscopes like HAYSTAC [15,16] or ADMX [17,18].

A broad region of UDM parameter space below the  $\mu\text{eV}$  range has been excluded indirectly through astrophysical probes [4,19] and tests of equivalence principle violations [20,21]. Beyond these limits, mechanical sensors are predestined to directly search for UDM fields in the kilohertz range [6,22]. The gravitational wave interferometers GEO600 [23] as well as LIGO and Virgo [24] provided broadband upper limits for scalar and vector UDM coupling by using the beam splitter and mirrors as susceptible elements. On the other hand, mechanical resonators with low dissipation can provide amplification of the signal to overcome technical noise and achieve thermal-noise limited readout close to their mode frequencies, at the cost of a small bandwidth. Remarkable sensitivities have been reached in cryogenic systems [25], such as the resonant-mass detector AURIGA, which set the strongest constraints on kilohertz scalar UDM to date [26]. Several tabletop mechanical sensors have been proposed to effectively probe scalar [22,27,28] and vector [29] UDM parameter space. Cavity optomechanical systems provide an ideal platform to sensitively probe the motion of such a mechanical sensor, using a microwave or optical readout mode [30]. Optomechanical transducers with quantum-limited sensitivity have been envisioned in various proposals for sub-GeV [6,31,32] and UDM detection [6,28,29,33,34].

Superfluid helium has been considered as a target material for particlelike sub-GeV DM in various proposals [31,35–39]

and has been used in experiments such as HERON [40], HeRALD [41,42], or DELight [43]. For UDM searches, superfluid  $^3\text{He}$  [44] and  $^4\text{He}$  [28] have been proposed as promising detection media. Here, we introduce HeLIOS (Helium ultraLIght dark matter Optomechanical Sensor)—the first UDM detector based on superfluid helium, capable of simultaneously searching for both scalar and vector bosons. Superfluid  $^4\text{He}$  is an ideal resonant mass for two reasons. First, it features ultralow dissipation at millikelvin temperatures, with demonstrated mechanical  $Q$  of more than  $10^8$  [45]. Second, helium is the only element that remains liquid at low temperatures. Consequently, it can be pressurized to continuously change the speed of sound and tune the acoustic mode frequencies up to 54%, thus overcoming the sensitivity-bandwidth trade-off and effectively enabling broadband detection [46,47]. Such tunability has already been recognized as a key detection feature, for example in the axion haloscopes [48,49] that employ frequency-tunable high- $Q$  microwave cavities.

## II. DETECTING ULTRALIGHT DARK MATTER WITH MECHANICAL SENSORS

In the standard halo model, DM has a Maxwellian velocity distribution [50], leading to a Doppler shift and broadening of the UDM frequency. This limits the coherence time to  $\tau_{\text{dm}} = 10^6/\omega_{\text{dm}}$  and coherence length to  $\lambda_{\text{dB}}$ , which exceeds 1000 km for frequencies less than 300 kHz [10]. Thus, the UDM field can be considered coherent for a million periods and spatially uniform for any lab-scale experiment probing the kilohertz range.

Scalar UDM could linearly couple to standard model (SM) fields, effectively leading to a modulation of the fine-structure constant or fermion masses [10]. This would result in a homogeneous strain  $h(t) = -dh_0 \cos(\omega_{\text{dm}}t)$  imposed on any condensed body, with dimensionless coupling strength  $d$  and amplitude  $h_0$  [22,28]. The oscillating strain acts as a driving force  $F_{\text{dm}}(t) = q_n \ddot{h}(t)$  when coupled to a narrow-band breathing mode  $n$  of a mechanical resonator, with normalized mode shape  $\tilde{\mathbf{u}}_n(\mathbf{x})$ , effective mass  $\mu_n = \int \rho |\tilde{\mathbf{u}}_n(\mathbf{x})|^2 d^3x$ , geometric mode overlap factor  $q_n = \int \rho \tilde{\mathbf{u}}_n(\mathbf{x}) \cdot \mathbf{x} d^3x$ , and mass density  $\rho$  [28,51].

On the other hand, vector UDM (or dark photons) could couple to SM fields through dark charges of an object, such as the baryon number  $B$  or baryon-minus-lepton number  $B - L$  [6]. In the center-of-mass frame, each object  $j$  would experience an acceleration  $\mathbf{a}_j(t) = f_j g \mathbf{a}_0 \cos(\omega_{\text{dm}}t)$ , with material-dependent suppression factor  $f_j$ , dimensionless coupling strength  $g$  and amplitude  $\mathbf{a}_0$  [29]. When acting on the mechanical modes of a resonator composed of two materials, the differential acceleration results in a driving force  $\mathbf{F}_{\text{dm}}(t) = \mu_n [\beta_{n,1} \mathbf{a}_1(t) + \beta_{n,2} \mathbf{a}_2(t)]$ , with geometric mode overlap factors  $\beta_{n,j} = \int_j \hat{\mathbf{a}} \cdot \tilde{\mathbf{u}}_n(\mathbf{x}) d^3x / \int_{1\cup 2} |\tilde{\mathbf{u}}_n(\mathbf{x})|^2 d^3x$  and acceleration polarization  $\hat{\mathbf{a}} = \mathbf{a}_0/|\mathbf{a}_0|$  [29].

Ultimately, detection requires a signal-to-noise ratio larger than unity. The signal force power spectral density (PSD)  $S_{FF}^{\text{dm}}$  for the respective UDM coupling [Eqs. (A2) and (A7)] as well as the considered noise contributions, adding up to the noise force PSD  $S_{FF}^{\text{noise}}$  [Eq. (A10)], are discussed in the Appendix. We assume the transduction to be ultimately limited by thermal noise on resonance and quantum noise off resonance, which has been demonstrated in several similar systems [52–55]. Equating both gives an estimate for the force sensitivity, i.e.,

$$S_{FF}^{\text{dm}}(\omega_{\text{dm}}) = S_{FF}^{\text{noise}}(\omega_{\text{dm}}) \sqrt{\frac{\tau_{\text{dm}}}{\tau}}, \quad (1)$$

for each normal mode (assuming no mode overlap). The factor  $\sqrt{\tau_{\text{dm}}/\tau}$  accounts for the noise reduction when estimating the incoherent signal PSD over long integration times  $\tau > \tau_{\text{dm}}$  through averaging  $\tau/\tau_{\text{dm}}$  independent periodograms [28,29,56].

We consider scalar UDM coupling to the electron mass  $m_e$  ( $d = d_{m_e}$ ) and vector UDM coupling to the baryon-minus-lepton number  $B - L$  ( $g = g_{B-L}$ ). However, the same approach can also constrain coupling to the fine-structure constant ( $d_e$ ) or baryon number ( $g_B$ ). Thus, HeLIOS can simultaneously search for UDM using four different DM-SM coupling channels.

Solving Eq. (1) for  $d_{m_e}$  or  $g_{B-L}$  yields the region of parameter space that HeLIOS could access when coupling to scalar or vector UDM, respectively. These are shown in Fig. 1 for the first ten normal modes of the prototype detector discussed below, including the extended regions when tuning the mode frequencies through pressurization as well as currently existing bounds. Although the optimal noise requirement has not been met yet, the projection is based on the measured parameters of the six characterized modes (listed in Table I and Appendix A 5). The scalar UDM sensitivity limit of this prototype is 2 orders of magnitude worse than the superfluid detector proposed in Ref. [28], which assumed a mechanical  $Q$  of  $10^9$  and a helium volume of almost 19 liters. Both assumptions are currently not realistic in our system.

## III. EXPERIMENTAL DESIGN

A sketch of the experiment is shown in Fig. 2. The design is similar to our previous prototype superfluid gravitational wave detector [47]. A commercial 2.75'' ConFlat nipple made of stainless steel provides a cylindrical volume for 145 ml of superfluid helium (with 12.8 cm length and 3.8 cm diameter). The bottom of the cell is capped by a ConFlat flange, while the top is sealed with a niobium membrane of 300  $\mu\text{m}$  thickness and 1.4 cm diameter, clamped from below through an indium-plated copper ring to facilitate a superfluid leak-tight cell.

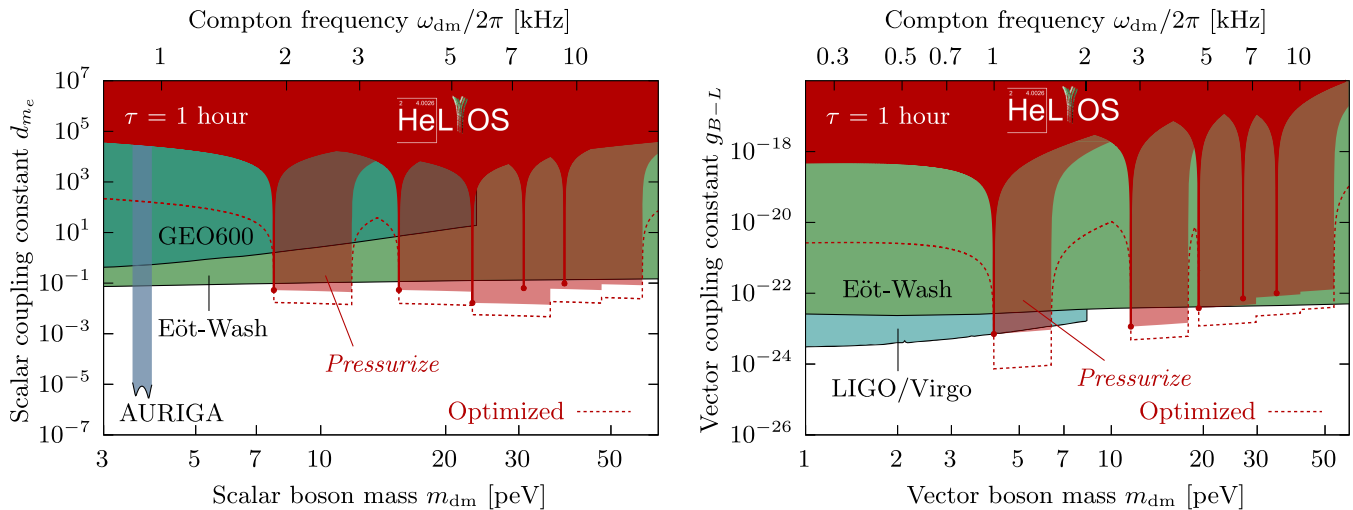


FIG. 1. Projected region of scalar UDM (left: coupling to the electron mass through  $d_{m_e}$ ) and vector UDM parameter space (right: coupling to the baryon-minus-lepton number through  $g_{B-L}$ ), accessible to the lowest ten modes of the current HeLIOS prototype with a quantum and thermal noise-limited transducer after  $\tau = 1$  hr integration time (solid red region with filled circles highlighting the on resonance reach), including frequency tuning through pressurization when integrating at each frequency for  $\tau = 1$  hr (transparent red). Although the noise limit has not been reached yet, this projection is based on the measured parameters of the six characterized modes (see Table I and Appendix A 5). Due to the convincing agreement of simulations and measurements, the remaining modes  $[r, \varphi, z] = [0, 0, 7]$  to  $[0, 0, 10]$  have only been simulated and a  $Q = 2.1 \times 10^6$  has been assumed, equal to the average measured  $Q$  of the first six modes. The dashed lines show limits achievable with realistic optimizations of the same design, achievable on the year timescale (using the temperature  $T = 10$  mK, microwave power  $P_c = 10$   $\mu$ W, microwave mode decay rate  $\kappa/2\pi = 1$  MHz, frequency shift  $\partial\omega_c/\partial P = -2\pi \times 2$  GHz/bar [47], and mechanical  $Q = 10^7$ ). Currently existing bounds by AURIGA [26], GEO600 [23], LIGO/Virgo [24], and the Eöt-Wash experiment [20,21] are shown in the background.

The kilohertz acoustic modes of the helium are non-resonantly coupled to the fundamental drum mode of the membrane, whose frequency is 16.2 kHz in the absence of helium. Mechanical dissipation of the resulting helium-membrane normal modes at millikelvin temperatures are dominated by losses in the membrane [45], which

TABLE I. Relevant parameters of the six lowest-order longitudinal acoustic helium modes  $[r, \varphi, z] = [0, 0, n]$  at saturated vapor pressure, coupled to the structural deformation of the membrane and detector body. Left: results from finite-element simulations for the mechanical frequencies  $f$ , effective masses  $\mu$  (normalized by the helium mass  $M = 21.0$  g), as well as geometric mode overlap factors  $q$  and  $\beta_{12}f_{12} = \beta_{n,1}f_1 + \beta_{n,2}f_2$  for coupling to scalar and vector UDM, respectively. Right: frequencies  $f$  and mechanical quality factors  $Q$  measured at a temperature of 20 mK.

Mode	Simulated				Measured	
	$f$ [Hz]	$\mu/M$	$q$ [gcm]	$\beta_{12}f_{12}$	$f$ [Hz]	$Q$ [ $10^6$ ]
[0, 0, 1]	933	0.50	2.97	$4.20 \times 10^{-2}$	998	0.26
[0, 0, 2]	1854	0.49	49.5	$1.63 \times 10^{-6}$	1864	2.2
[0, 0, 3]	2785	0.47	1.26	$1.44 \times 10^{-2}$	2800	3.7
[0, 0, 4]	3712	0.43	42.6	$2.70 \times 10^{-6}$	3729	1.9
[0, 0, 5]	4648	0.42	2.55	$0.90 \times 10^{-2}$	4668	2.2
[0, 0, 6]	5589	0.40	103	$2.38 \times 10^{-6}$	5605	2.6

were reduced through annealing and electropolishing the niobium plate [57].

The top side of the membrane forms half of a superconducting cylindrical reentrant microwave cavity made of indium-plated copper [see Fig. 2(b)], similar to the one used in Refs. [58,59] (see Appendix A 5 for more information). A central stub confines the electric field within a small gap to the membrane (100  $\mu$ m). The helium pressure strongly modulates the frequency of the microwave resonator through the capacitance, enabling sensitive optomechanical transduction of the helium motion. Driving the microwave cavity on resonance encodes the mechanical motion into the phase of the transmitted signal, which is amplified through a cryogenic HEMT and down-converted using a standard homodyne circuit illustrated in Fig. 2(a). A piezoelectric transducer is affixed to the bottom blank of the cell to facilitate coherent excitation of the mechanical modes.

The helium cell is suspended from the mixing chamber plate of a wet dilution refrigerator through a series of four alternating copper masses and springs to isolate the detector from mechanical vibrations [60,61] (see Appendix A 6 for more information). The helium fill line is thermalized through sintered heat exchangers on each stage of the dilution refrigerator, enabling a base temperature of 20 mK as measured through a primary nuclear orientation thermometer.

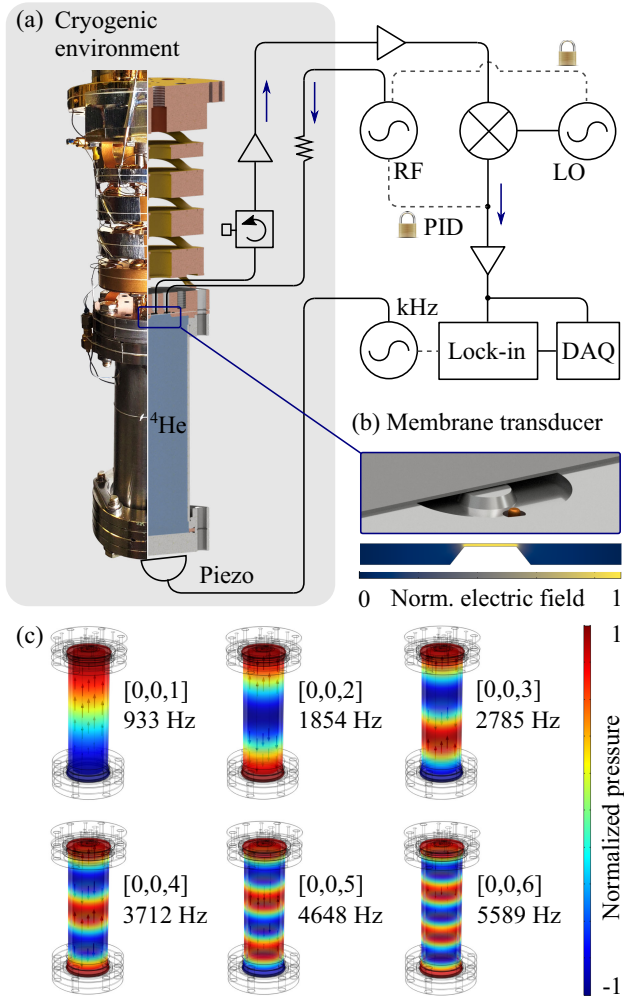


FIG. 2. (a) Experimental setup, including a picture and cut rendering of the detector assembly suspended from the mixing chamber of a dilution refrigerator as well as a sketch of the readout electronics. (b) Rendering of the reentrant microwave cavity transducer with a membrane as interface to the helium (cut in half for illustration purposes). (c) Finite-element simulations of the lowest-order mechanical modes along the cylinder axis  $[r, \varphi, z] = [0, 0, n]$ , with the normalized acoustic pressure fields of the helium and computed mode frequencies.

#### IV. CHARACTERIZATION

Figure 2(c) shows finite-element simulations of the six lowest-order acoustic pressure modes  $[r, \varphi, z] = [0, 0, n]$ , mechanically coupled to the structural modes of the membrane and surrounding detector body. Their computed frequencies, effective masses, as well as geometric mode overlap factors for coupling to scalar and vector UDM are shown in Table I.

Only the even-ordered breathing modes  $n \in \{2, 4, 6\}$  feature a significant mode overlap factor  $q_n$  for coupling to scalar UDM, with  $q_6$  being the largest as a result of the spectral vicinity of  $[0, 0, 6]$  to the structural breathing mode of the cell, which finite-element modeling shows has a

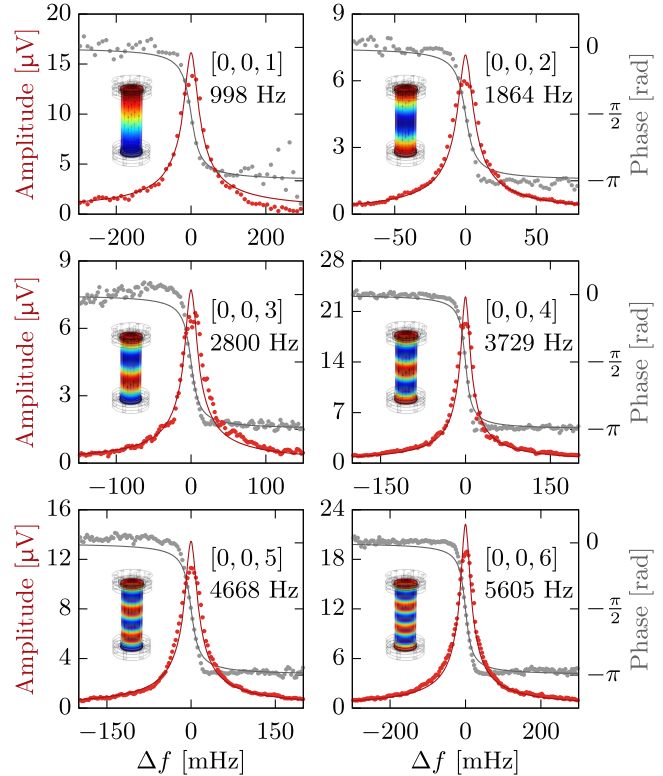


FIG. 3. Lock-in amplitude and phase of the six lowest-order mechanical modes along the cylinder axis  $[r, \varphi, z] = [0, 0, n]$ , measured at a temperature of 20 mK and helium pressure of 170 mbar for  $[0, 0, 1]$  to  $[0, 0, 3]$  as well as 70 mbar for  $[0, 0, 4]$  to  $[0, 0, 6]$ . The quoted frequencies are extrapolations to the helium saturated vapor pressure of  $\approx 0$  mbar, using the linear regressions obtained in Fig. 4.

frequency of 5.3 kHz. On the other hand, only the odd-ordered modes  $n \in \{1, 3, 5\}$  will couple to vector UDM with a substantial  $\beta_{n,12} f_{12} = \beta_{n,1} f_1 + \beta_{n,2} f_2$ , as a result of the differential acceleration between helium ( $f_1 = -3.29 \times 10^{-2}$ ) and stainless steel detector body ( $f_2 = 0.07 \times 10^{-2}$ ). Thus, HeLIOS could simultaneously search for both scalar and vector UDM, with an equal amount of susceptible modes.

After filling the cell completely with 145 ml superfluid helium and reaching a final base temperature of 20 mK, the six lowest-order mechanical modes were characterized by sweeping the piezo drive frequency and coherently measuring the transmitted microwave phase with a lock-in amplifier. Figure 3 shows the resulting amplitude and phase spectra for the modes  $[0, 0, 1]$  to  $[0, 0, 6]$ . Only the measured mode frequency of the fundamental mode  $[0, 0, 1]$  deviates appreciably (by 7.0%) from the simulated one. This is likely a result of hybridization with another low- $Q$  mechanical mode in its spectral vicinity that could originate from the detector or suspension structure. Mechanical quality factors were obtained through ring-down measurements at a pressure of 220 mbar and are also

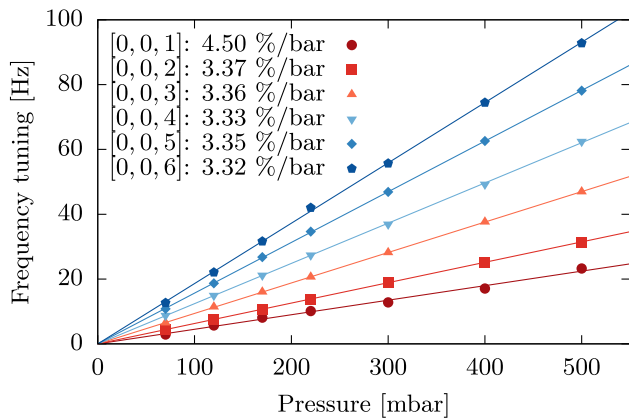


FIG. 4. Frequency tuning of the six lowest-order mechanical modes along the cylinder axis  $[r, \varphi, z] = [0, 0, n]$  through pressurization of the helium at a temperature of 20 mK, relative to the zero-pressure frequency  $f_0$ . Solid lines show linear regressions, with relative slopes (normalized to  $f_0$  of each mode) quoted in the legend.

shown in Table I. Low dissipation is found, with  $Q$  values between 1.9 and 3.7 million, except for  $[0, 0, 1]$  with  $Q = 2.6 \times 10^5$ .

Finally, the helium pressure was swept from  $P = 70$  to 500 mbar to demonstrate the frequency tunability of the mechanical modes. Figure 4 shows the frequency shift obtained for the six lowest-order modes. The tuning in this pressure range is approximately linear, with regressions yielding slopes of  $3.35 \pm 0.03\%/bar$  for all modes except  $[0, 0, 1]$ . These results agree well with the relative change of the helium first sound velocity in this pressure range of  $\Delta c_{\text{He}}/\Delta P c_{\text{He}} = 3.55\%/bar$  [46,62]. The cell proved to be superfluid leak tight to at least 7 bar. A maximum frequency shift of up to 54 % would be achievable at the helium solidification pressure of 25 bar. The discrepancy of the  $[0, 0, 1]$  mode in quality factor and frequency tunability is consistent with its larger frequency, supporting the assumption of an unintended mode hybridization.

In this implementation, no thermally driven mechanical modes could be observed up to 480 mK when applying  $P_c \approx 10$  nW microwave power. Using Eqs. (A8) and (A9) from Appendix A 3, with cavity loss rate  $\kappa/2\pi = 11$  MHz and optomechanical coupling rate  $|g_0|/2\pi \lesssim 2.5$   $\mu\text{Hz}$ , we find that the imprecision noise limit is up to 13 dB above the thermal noise floor on resonance (backaction is negligible). Relatively small improvements of the transducer could significantly lower  $S_{xx}^{\text{imp}} \sim \kappa^2/g_0^2$ . These include optimizing the microwave cavity geometry, material, fabrication, and coupling to at least achieve  $\kappa/2\pi = 2$  MHz and  $g_0/2\pi = 28$   $\mu\text{Hz}$ , which we already demonstrated in our previous detector prototype that was capable to observe thermally driven motion [47]. Above  $\approx 100$  mK, increasing three-phonon dissipation limits the ability to resolve the

superfluid acoustic modes [63]. Thermal noise-limited readout would facilitate displacement calibration of the time domain signal [64], enabling the conversion of the measured noise spectrum to bounds on the UDM coupling constants.

## V. DISCUSSION

Here, we have introduced the superfluid helium UDM detector HeLIOS and demonstrated its working principle. The mechanical modes could be characterized when coherently driven, featuring high quality factors and frequency tunability when pressurized. Once optimized and calibrated, the detector could scan the accessible frequency range for the expected Doppler-broadened UDM signal shape [10,26]. Detection protocols and false-signal tests similar to the ones used by current axion haloscope experiments like HAYSTAC [49] or ADMX [48] could be used, as their bandwidth also relies on the continuous tunability of high- $Q$  resonant modes. The minimum time required to scan the accessible frequency range (with  $\tau = \tau_{\text{dm}} \sim 1$  min) is around 100 days, while it would take almost eight years when integrating for  $\tau = 1$  hour at each frequency, as proposed in Fig. 1 (see Appendix A 4 for more information).

Importantly, Fig. 1 illustrates the promise of this approach for realistically achievable experimental parameters, providing a pathway to simultaneously search for dark matter via four different SM coupling channels after only an hour of integration time. After optimizing the optomechanical transduction to observe thermally driven mechanics and improve off resonance sensitivity, future generations also have room to decrease the thermal noise floor reached on resonance. We think that a mechanical  $Q$  of  $10^7$ , a base temperature of 10 mK, and a helium volume of around one liter represent realistic next-generation improvements, readily constructed on the year timescale. The dashed lines in Fig. 1 show the accessible regions of UDM parameter space for an optimized detector with unchanged dimensions, while a sensitivity improvement over several orders of magnitude is projected in Appendix A 9 for future generations with up-scaled helium volumes—illustrating that HeLIOS could soon be able to effectively probe unconstrained regions of UDM parameter space. As a long-term goal, the reduction of technical noise contributions could be sufficient to achieve an off resonance sensitivity below currently existing bounds, facilitating broadband detection at any helium pressure, with a significantly wider bandwidth than the current prototype. In addition, mitigating technical and quantum noise and probing helium physics in HeLIOS will also inform other helium-based searches of both wavelike and particlelike light dark matter.

## ACKNOWLEDGMENTS

The authors would like to thank Samy Boutros, Kripa Vyas, and Brigitte Vachon for fruitful discussions. They acknowledge that the land on which this work was performed is in Treaty Six Territory, the traditional territories of many First Nations, Métis, and Inuit in Alberta. Moreover, they acknowledge support from the University of Alberta; the Natural Sciences and Engineering Research Council, Canada (Grants No. RGPIN-2022-03078 and No. CREATE-495446-17); the Arthur B. McDonald Canadian Astroparticle Physics Research Institute through the support of the Canada First Research Excellence Fund; the National Science Foundation Grants No. PHY-1912480 and No. PHY-2047707; and the Office of the Under Secretary of Defense for Research and Engineering under Grant No. FA9550-22-1-0323.

## APPENDIX

### 1. Scalar UDM coupling to mechanical resonators

Linear coupling of scalar UDM to SM particles would cause a sinusoidal modulation of the fine-structure constant  $\alpha$  or fermion masses at the UDM Compton frequency  $\omega_{\text{dm}}$  [22]. Since the Bohr radius  $a_0$  scales inversely proportional to  $\alpha$  and the electron mass  $m_e$ , this results in a spatially uniform strain

$$h(t) = -dh_0 \cos(\omega_{\text{dm}}t) \quad (\text{A1})$$

acting on a liquid or solid, with dimensionless coupling strength  $d$  and amplitude  $h_0 = \sqrt{8\pi G Q_{\text{dm}}}/c\omega_{\text{dm}} \approx 1.1 \times 10^{-15} \text{ s}^{-1}/\omega_{\text{dm}}$  (with local DM density  $Q_{\text{dm}}$ ) [28].

The strain signal leads to an amplified displacement  $\mathbf{u}_n(\mathbf{x}, t) = \tilde{\mathbf{u}}_n(\mathbf{x})\xi_n(t)$  when resonantly coupled to a breathing mode  $n$  of a mechanical resonator with mode shape  $\tilde{\mathbf{u}}_n(\mathbf{x})$ , normalized by the maximum amplitude  $\xi_n(t)$ . The latter can be modeled as an effective harmonic oscillator that is driven by the UDM force  $F_{\text{dm}}(t) = q_n \ddot{h}(t)$ , with geometric mode overlap factor  $q_n = \int \rho \tilde{\mathbf{u}}_n(\mathbf{x}) \cdot \mathbf{x} d^3x$  and mass density of the detector material  $\rho$  [28,51]. Including the finite linewidth due to the UDM coherence time  $\tau_{\text{dm}}$ , the peak PSD of the scalar UDM force acting on the mode reads as

$$S_{FF}^{\text{dm}}(\omega_{\text{dm}}) = (q_n dh_0)^2 \omega_{\text{dm}}^4 \tau_{\text{dm}}. \quad (\text{A2})$$

### 2. Vector UDM coupling to mechanical resonators

Vector UDM could couple to SM fields through the baryon number  $B$  or baryon-minus-lepton number  $B - L$  of an object [6]. Considering the latter, a free-falling material  $j$  with average proton-to-nucleon ratio  $Z_j/A_j$  of its atoms will experience the acceleration

$$\tilde{\mathbf{a}}_j(t) = \left(1 - \frac{Z_j}{A_j}\right) g \mathbf{a}_0 \cos(\omega_{\text{dm}}t), \quad (\text{A3})$$

with dimensionless coupling strength  $g$  and amplitude  $|\mathbf{a}_0| = \sqrt{2e^2 Q_{\text{dm}}/\epsilon_0 m_n^2} \approx 3.7 \times 10^{11} \text{ m/s}^2$  (using the nucleon mass  $m_n$ ) [29]. The c.m. acceleration of two bodies with masses  $m_j$  reads as  $\mathbf{a}_{\text{c.m.}}(t) = [m_1 \tilde{\mathbf{a}}_1(t) + m_2 \tilde{\mathbf{a}}_2(t)]/M$  (with total mass  $M = m_1 + m_2$ ). Consequently, the acceleration of each object in the c.m. frame is given through

$$\mathbf{a}_j(t) = \tilde{\mathbf{a}}_j(t) - \mathbf{a}_{\text{c.m.}}(t) = f_j g \mathbf{a}_0 \cos(\omega_{\text{dm}}t), \quad (\text{A4})$$

where we introduced the suppression factor

$$f_j = \frac{m_1 Z_1}{MA_1} + \frac{m_2 Z_2}{MA_2} - \frac{Z_j}{A_j} = \begin{cases} \frac{m_2}{M} \left( \frac{Z_2}{A_2} - \frac{Z_1}{A_1} \right) & \text{for } j = 1 \\ \frac{m_1}{M} \left( \frac{Z_1}{A_1} - \frac{Z_2}{A_2} \right) & \text{for } j = 2, \end{cases} \quad (\text{A5})$$

quantifying the  $B - L$  mismatch of two materials to obtain a differential acceleration. In the limit  $m_2 \gg m_1$ , the c.m. of both objects coincides with the c.m. of the second material, and the suppression factors become  $f_1 \approx [(Z_2/A_2) - (Z_1/A_1)]$  and  $f_2 \approx 0$ , consistent with Ref. [29].

The fraction of UDM acceleration that couples to the normal mode  $n$  of a mechanical resonator with effective mass  $\mu_n = \int \rho |\tilde{\mathbf{u}}_n(\mathbf{x})|^2 d^3x$  is given through the overlap integral [29]

$$\begin{aligned} \frac{F_{\text{dm}}(t)}{\mu_n} &= \frac{\int_{1\cup 2} \mathbf{a}(t) \cdot \tilde{\mathbf{u}}_n(\mathbf{x}) d^3x}{\int_{1\cup 2} |\tilde{\mathbf{u}}_n(\mathbf{x})|^2 d^3x} \\ &= \sum_{j=1}^2 \underbrace{\frac{\int_j \hat{\mathbf{a}} \cdot \tilde{\mathbf{u}}_n(\mathbf{x}) d^3x}{\int_{1\cup 2} |\tilde{\mathbf{u}}_n(\mathbf{x})|^2 d^3x}}_{=\beta_{n,j}} a_j(t) \\ &= \underbrace{(\beta_{n,1} f_1 + \beta_{n,2} f_2)}_{=\beta_{n,12} f_{12}} g \mathbf{a}_0 \cos(\omega_{\text{dm}}t), \end{aligned} \quad (\text{A6})$$

where we defined the geometric mode overlap factors  $\beta_{n,j}$ . The UDM polarization  $\hat{\mathbf{a}} = \mathbf{a}_0/|\mathbf{a}_0|$  varies over  $\tau_{\text{dm}}$ , such that it averages to  $\langle a^2 \rangle \rightarrow \langle a^2 \rangle/3$  when observed with a static detector over many coherence times [29]. In this case, the peak vector UDM driving force PSD becomes

$$S_{FF}^{\text{dm}}(\omega_{\text{dm}}) = \frac{1}{3} (\mu_n \beta_{n,12} f_{12} g |\mathbf{a}_0|)^2 \tau_{\text{dm}}. \quad (\text{A7})$$

### 3. Detector noise contributions

The respective UDM-induced driving force (A2) or (A7) has to compete with all contributions to the detector noise. When using the acoustic modes of a test mass, thermal

noise imposes a fundamental limitation regardless of the readout mechanism. The force PSD in the vicinity of a normal mode  $n$  with effective mass  $\mu_n$ , frequency  $\Omega_n$ , and mechanical quality factor  $Q_n$  is approximately white and reads as [25]

$$S_{FF}^{\text{th}} = \frac{4k_B T \mu_n \Omega_n}{Q_n}. \quad (\text{A8})$$

For a given resonator, it can only be reduced through low temperatures  $T$  and low dissipation (i.e., high  $Q_n$ ). This favors the use of superfluid helium as resonant mass, featuring ultralow dissipation limited only through three-phonon scattering and He-3 impurities below  $\approx 600$  mK [63], with demonstrated mechanical quality factors of more than  $10^8$  [45].

Cavity optomechanical transducers exploit the frequency dependence of the circulating optical or microwave mode to a mechanical quantity, like the displacement of a cavity mirror [30]. Thereby, a weak signal of a mechanical mode can be parametrically up-converted, with an enhanced gain through a large photon occupation in the cavity. The displacement sensitivity is ideally limited through quantum noise—shot noise (with displacement PSD  $S_{xx}^{\text{imp}}$ ) and back-action noise (with force PSD  $S_{FF}^{\text{ba}}$ ) [65]. For an overcoupled cavity with total (external) cavity decay rate  $\kappa$  ( $\kappa_{\text{ext}}$ ) satisfying  $\kappa \approx \kappa_{\text{ext}} \gg \Omega_n$ , these can be expressed as [66]

$$S_{xx}^{\text{imp}} = \frac{\hbar^2}{S_{FF}^{\text{ba}}} = \frac{\kappa}{8n_c G^2}, \quad (\text{A9})$$

where  $n_c = 4P_c/\kappa\hbar\omega_c$  is the average cavity photon occupation (for circulating power  $P_c$  and frequency tuned to the cavity resonance  $\omega_c$ ) and  $G = \partial\omega_c/\partial x$  describes the coupling rate with mirror displacement  $x$  [30].

Finally, the force PSD  $S_{FF}^{\text{noise}}(\omega)$  as a function of frequency  $\omega$  for all considered noise contributions (A8) and (A9) adds up to

$$S_{FF}^{\text{noise}}(\omega) = S_{FF}^{\text{th}} + |\chi(\omega)|^{-2} S_{xx}^{\text{imp}} + S_{FF}^{\text{ba}}, \quad (\text{A10})$$

using the mechanical susceptibility  $\chi(\omega) = [\mu_n(\Omega_n^2 - \omega^2 + i\omega\Omega_n/Q_n)]^{-1}$ . We stress that this expression only reflects the limiting noise contributions. Other technical noise sources include mechanical vibrations exceeding the filter capabilities of the suspension discussed in Appendix A 6, Johnson-Nyquist noise of higher-temperature electronics, crosstalk, and interference due to impedance mismatches.

Figure 5 compares the undriven signal PSD of the  $[0, 0, 2]$  mode with the signal measured when a chirp drive is applied through the piezo. The white noise floor and absence of a mechanical response when undriven illustrate that the detector is limited by frequency-independent imprecision noise (shot noise or other electronic noise), obscuring the thermally driven mechanics.

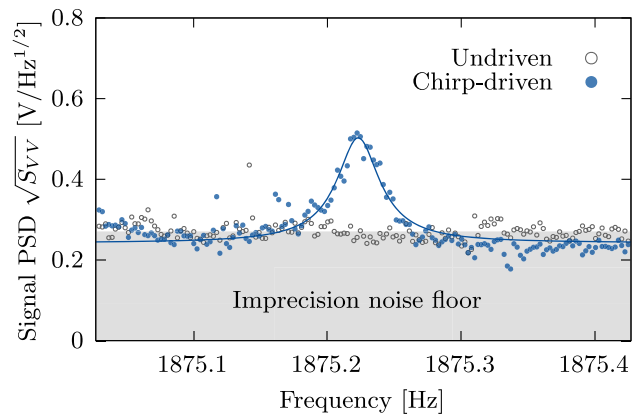


FIG. 5. Voltage power spectral density of the  $[0, 0, 2]$ -mode measured with and without a 50 Hz-bandwidth chirp drive applied through the piezo. The solid line shows a Lorentzian regression to the driven data. Each time-domain dataset was acquired for 11.4 hrs after filtering with a lock-in amplifier referenced to 1875 Hz.

#### 4. Total integration time for a detection run

For each helium pressure  $P$ , averaging  $\tau/\tau_{\text{dm}}$  periodograms of the homodyne signal after a total integration time  $\tau$  results in a noise floor with sharp minima at the mechanical resonance frequencies  $\Omega_n(P)$  (as shown in solid red in Fig. 1). When sweeping the pressure to 25 bar, the frequencies can be tuned to  $\Omega_{n,\text{max}}$ , which are 54% above the frequencies at saturated vapor pressure  $\Omega_{n,\text{min}}$  [46]. To be able to resolve the UDM signal with linewidth  $1/\tau_{\text{dm}} = \omega/10^6$ , a minimum integration time of  $\tau \geq \tau_{\text{dm}}$  and maximum frequency tuning step of  $\delta\omega \leq 1/\tau_{\text{dm}}$  is required.

Since  $\delta\omega \ll \Omega_{n,\text{max}} - \Omega_{n,\text{min}}$ , the total time for a frequency sweep can be estimated as

$$\tau_{\text{tot}} = \max_n \int_{\Omega_{n,\text{min}}}^{\Omega_{n,\text{max}}} \frac{\tau(\omega)}{\delta\omega(\omega)} d\omega, \quad (\text{A11})$$

which yields a minimum time of  $\tau_{\text{tot}} = 103$  days for  $\tau = \tau_{\text{dm}}$  (i.e., only one periodogram for each scan instead of averaging) and a total time of  $\tau_{\text{tot}} = 2863$  days  $\approx 7.8$  years for  $\tau = 1$  hour, which is required to achieve the limits shown in Fig. 1. The duration of a complete detection run is limited by the data acquisition (as stated above), not by the data analysis, which can be performed simultaneously.

#### 5. Microwave optomechanical transducer

The cylindrical reentrant microwave cavity of the current HeLIOS prototype has a frequency of  $\omega_c/2\pi = 11.5$  GHz and total cavity decay rate of  $\kappa/2\pi = 11$  MHz ( $Q_c = \omega_c/\kappa = 1040$ ). Due to unavoidable seam losses and surface losses at the highly confined electric field, dissipation around this order of magnitude is expected for a reentrant

microwave cavity with a similar geometry [58,59]. However, the employed indium-plated copper cavity featured a larger decay rate than the aluminum cavity of our previous superfluid detector [47], possibly resulting from a poor indium layer quality or differential thermal contraction between the indium and copper.

When the helium applies a pressure  $P$ , the frequency of the microwave resonator is strongly modulated with a coupling rate of  $\partial\omega_c/\partial P = -2\pi \times 374$  MHz/bar. Consequently, the single-photon single-phonon coupling rate lies between  $g_0 = (\partial\omega_c/\partial P)\Delta P_{ZP} = -2\pi \times 1.0$   $\mu$ Hz and  $-2\pi \times 2.5$   $\mu$ Hz for the first six longitudinal modes, with zero point displacement amplitudes  $x_{ZP} = \sqrt{\hbar/2\mu_n\Omega_n} \sim 10^{-19}$  m or pressure fluctuations  $\Delta P_{ZP} = \sqrt{\hbar\Omega_n/\kappa_{\text{He}}V_{\text{eff},n}} \sim 10^{-10}$  Pa, helium compressibility  $\kappa_{\text{He}} = 1.2 \times 10^{-7}$  Pa $^{-1}$ , and effective volume  $V_{\text{eff},n}$  of the respective mode pressure field [67].

In this characterization, a microwave power of  $P_c \approx 10$  nW has been applied. The current setup with 65 dB input attenuation in the cryostat allows for a maximum power of 1  $\mu$ W at the microwave cavity. An improved cryogenic wiring with reduced dissipation would allow for 10  $\mu$ W microwave drive tones in future iterations. In any case, the small microwave dissipation  $\sim P_c\kappa_{\text{int}}/\kappa \ll P_c$  in an overcoupled cavity ( $\kappa_{\text{int}} \ll \kappa$ ) would cause a negligible heat leak compared to the  $\approx 1$   $\mu$ W cooling power at the mixing chamber stage.

## 6. Suspension

To isolate the detector from mechanical vibrations, a series of four alternating copper masses and springs suspends the helium cell and microwave transducer from the mixing chamber plate of a dilution refrigerator [60,61]. Each mass-spring unit cell—with a free frequency of  $\approx 60$  Hz—acts as a second-order mechanical low-pass filter [60], with a measured average attenuation of  $-16$  dB between the  $-3$  dB cutoff frequency of 860 Hz and 10 kHz. Figure 6 shows a finite-element simulation of the acceleration transfer function through the suspension, with the number of mechanical normal modes and the steepness of the high-frequency roll-off increasing with the number of unit cells. The cantilever springs of 0.5 and 0.6 mm thickness also facilitate thermal conduction to the detector assembly.

## 7. Acoustic modes in a cylinder

Considering only the superfluid, each acoustic pressure mode  $[r, \varphi, z] = [0, 0, n]$  along the cylinder axis of the detector (with length  $L = 12.8$  cm and  $z \in [-L/2, L/2]$ ) can be approximated as a solution to a one-dimensional wave equation, yielding

$$P_n(z, t) = \cos\left[k_n\left(z + \frac{L}{2}\right)\right] \Delta P_n \sin(\Omega_n t), \quad (\text{A12})$$

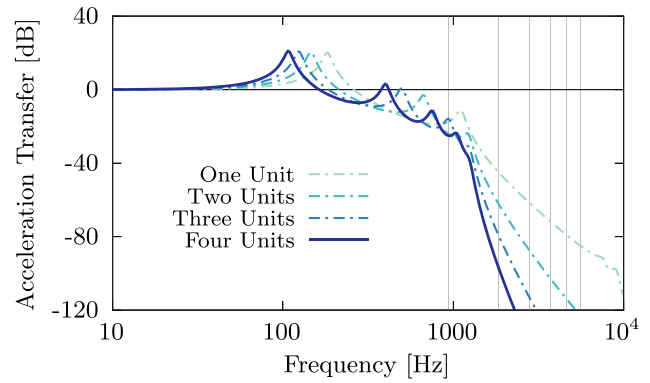


FIG. 6. Finite-element simulated transfer functions of the vertical acceleration measured below the suspension with one to four mass-spring unit cells, normalized by the acceleration above the top spring. The lowest-order mechanical mode frequencies of HeLIOS are indicated as vertical lines.

with acoustic pressure amplitude  $\Delta P_n$  at the membrane, wave number  $k_n = \pi n/L$ , frequency  $\Omega_n = 2\pi f_n = c_{\text{He}}k_n$ , and helium first sound velocity at saturated vapor pressure  $c_{\text{He}} = 238$  m/s [62] (leading to  $f_n \approx n \times 930$  Hz). Similarly, the displacement field in the  $z$  direction reads as

$$u_n(z, t) = - \underbrace{\sin\left[k_n\left(z + \frac{L}{2}\right)\right]}_{=\tilde{u}_n(z)} \Delta u_n \sin(\Omega_n t), \quad (\text{A13})$$

with displacement amplitude  $\Delta u_n$ . The sinusoidal mode profile  $\tilde{u}_n(z)$  would lead to a mode-independent effective mass of  $\mu_n = \int \rho |\tilde{u}_n(z)|^2 d^3x = M/2$ , i.e., equal to half of the geometric helium mass  $M = 21.0$  g. Moreover, the geometric mode overlap factors would be equal to

$$q_n = \int \rho \tilde{u}_n(z) z d^3x = \begin{cases} 0 & \text{for odd } n \\ M/k_n & \text{for even } n, \end{cases} \quad (\text{A14})$$

for coupling to scalar UDM (with  $M/k_n \approx 86$  g cm/ $n$ ), and

$$\beta_{n,\text{He}} = \frac{\int \tilde{u}_n(z) d^3x}{\int |\tilde{u}_n(z)|^2 d^3x} = \begin{cases} -4/\pi n & \text{for odd } n \\ 0 & \text{for even } n \end{cases}, \quad (\text{A15})$$

for coupling to vector UDM with polarization  $\hat{a} = \hat{z}$ . Using the suppression factors as defined in Eq. (A5), one obtains  $\beta_{n,12}f_{12} = \sum_{j=1}^2 \beta_{n,j}f_j \approx -4f_{\text{He}}/\pi n \approx 4.28 \times 10^{-2}/n$  in the limit  $m_{\text{SS}} \gg m_{\text{He}}$ , i.e., assuming a heavy stainless steel cell structure.

The obtained frequencies, effective masses, and most geometric mode overlap factors agree well with the ones computed through simulations of the entire assembly, as shown in Fig. 2(c) and Table I of the main text. This underlines the fact that the modes are heliumlike, i.e., most of the energy is stored in the acoustic modes of the superfluid. Discrepancies are the results of coupling to the

membrane and detector body (particularly for  $q_4$  and  $q_6$ , as the frequency of the cell's fundamental breathing mode is approached), as well as the three-dimensional nature of the displacement fields.

### 8. Membrane characterization

After cooling the detector to 30 mK, the free membrane motion was characterized by sweeping the piezo drive frequency and coherently measuring the transmitted microwave phase with a lock-in amplifier, revealing a fundamental drum mode with frequency  $f_{\text{mem}} = 16.2$  kHz. To quantify dissipation, ring-down measurements were conducted by repeatedly driving the membrane on resonance and subsequently observing the amplitude freely decaying according to  $A(t) \propto \exp(-\pi f_{\text{mem}} t/Q)$ , yielding a mechanical quality factor of  $Q = 5.6 \times 10^4$ .

### 9. Scaling opportunity

For future detector generations, there is the opportunity to reach substantially improved sensitivities to UDM by up-scaling the superfluid helium volume. Assuming that the mode frequencies  $f \propto 1/L$ , effective masses  $\mu \propto R^2 L$ , and geometric mode overlap factors  $q \propto R^2 L^2$  are dominated by the helium acoustics, they can be analytically computed for a cylindrical helium cell with radius  $R$  and length  $L$  (using the equations derived in Appendix A 7).

Eventually, on resonance limits set on the scalar UDM coupling constant  $d_{m_e}$  scale as  $\propto 1/RL^{5/4}$ . Figure 7 shows the resulting parameter space projection accessible with detector geometries ranging from the current prototype (as presented in Fig. 1) and a helium cell with the size of the AURIGA gravitational wave detector ( $\approx 830$  liter superfluid capacity) [68].

The coupling of vector UDM to the acoustic modes of the superfluid benefits from the same scaling law  $g \propto 1/RL^{5/4}$ , yielding improvements of the parameter space limits comparable to the ones shown in Fig. 7. On top of that, vector UDM coupling can be increased through careful selection of the cell material to maximize the suppression factor  $f_{\text{He}}$ . For a negligible helium mass,  $|f_{\text{He}}| \approx |(Z/A) - (1/2)|$  [see Eq. (A5)] essentially quantifies the proton-to-neutron mismatch of the detector material with average proton number  $Z$ , neutron number  $N$ , and atomic

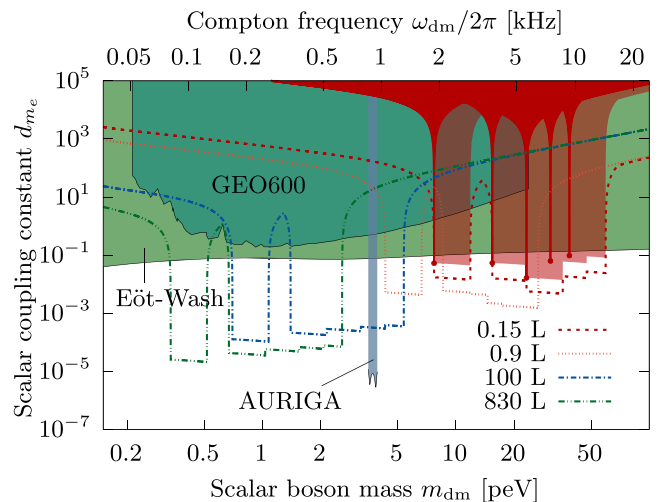


FIG. 7. Projected limits on the scalar UDM coupling constant  $d_{m_e}$  achievable through scaled-up cylindrical helium volumes, using the optimized parameters listed in the caption of Fig. 1. The red shaded region and dashed line (optimized) correspond to the limits achievable with the current prototype geometry (radius  $R = 1.9$  cm, length  $L = 12.8$  cm, and  $V = 0.15$  liter helium capacity; equivalent to Fig. 1). The orange, blue, and green dashed lines show estimated sensitivities for the second generation HeLIOS prototype ( $R = 5$  cm,  $L = 11.5$  cm,  $V = 0.9$  L; under development; finite-element simulation), a 100-liter superfluid detector ( $R = 15$  cm,  $L = 141$  cm), and a helium cell with the dimensions of the AURIGA Weber bar ( $R = 30$  cm,  $L = 294$  cm,  $V = 830$  L [68]), respectively. Currently existing bounds by AURIGA [26], GEO600 [23], and the Eöt-Wash experiment [21] are shown in the background.

mass  $A = Z + N$ —naturally favoring heavy elements. For example, a dominating lead mass rigidly attached to the cell would yield a suppression factor of  $|f_{\text{He}}| \approx 0.104$ , around 3 times larger as  $|f_{\text{He}}| \approx 0.034$  for stainless steel. Since  $(S_{FF}^{\text{dm}})^{1/2} \propto |f_{\text{He}}|$ , the limits on the coupling constant  $g$  would scale inversely proportional to  $|f_{\text{He}}|$ .

Major limitations of the detector size are the space constraints and cooling capabilities of the cryostat. However, customized dilution refrigerators with base temperatures in the mK range can be constructed for large-scale experiments, such as the AURIGA Weber bar or the SuperCDMS dark matter detector [52,69,70].

- [1] J. A. Tyson, G. P. Kochanski, and I. P. Dell’Antonio, Detailed mass map of CL 0024 + 1654 from strong lensing, *Astrophys. J.* **498**, L107 (1998).  
 [2] M. Markevitch, A. Gonzalez, D. Clowe, A. Vikhlinin, W. Forman, C. Jones, S. Murray, and W. Tucker, Direct constraints on the dark matter self-interaction cross section

from the merging galaxy cluster 1E 0657–56, *Astrophys. J.* **606**, 819 (2004).

- [3] N. Aghanim, Y. Akrami, M. Ashdown, J. Aumont, C. Baccigalupi, M. Ballardini, A. Banday, R. Barreiro, N. Bartolo, S. Basak *et al.*, Planck 2018 results-VI. Cosmological parameters, *Astron. Astrophys.* **641**, A6 (2020).

- [4] W. Hu, R. Barkana, and A. Gruzinov, Fuzzy cold dark matter: The wave properties of ultralight particles, *Phys. Rev. Lett.* **85**, 1158 (2000).
- [5] B. Carr, F. Kühnel, and M. Sandstad, Primordial black holes as dark matter, *Phys. Rev. D* **94**, 083504 (2016).
- [6] D. Carney, G. Krnjaic, D. C. Moore, C. A. Regal, G. Afek, S. Bhave, B. Brubaker, T. Corbitt, J. Cripe, N. Crisosto *et al.*, Mechanical quantum sensing in the search for dark matter, *Quantum Sci. Technol.* **6**, 024002 (2021).
- [7] Y. Hochberg, Y. F. Kahn, R. K. Leane, S. Rajendran, K. Van Tilburg, T.-T. Yu, and K. M. Zurek, New approaches to dark matter detection, *Nat. Rev. Phys.* **4**, 637 (2022).
- [8] D. F. Jackson Kimball and K. Van Bibber, *The Search for Ultralight Bosonic Dark Matter* (Springer Nature, Cham, Switzerland, 2023).
- [9] D. Antypas, A. Banerjee, C. Bartram, M. Baryakhtar, J. Betz, J. J. Bollinger, C. Boutan, D. Bowring, D. Budker, D. Carney *et al.*, New horizons: Scalar and vector ultralight dark matter, [arXiv:2203.14915](https://arxiv.org/abs/2203.14915).
- [10] A. Derevianko, Detecting dark-matter waves with a network of precision-measurement tools, *Phys. Rev. A* **97**, 042506 (2018).
- [11] A. Arvanitaki, J. Huang, and K. Van Tilburg, Searching for dilaton dark matter with atomic clocks, *Phys. Rev. D* **91**, 015015 (2015).
- [12] Y. V. Stadnik and V. V. Flambaum, Searching for dark matter and variation of fundamental constants with laser and maser interferometry, *Phys. Rev. Lett.* **114**, 161301 (2015).
- [13] Y. V. Stadnik and V. V. Flambaum, Can dark matter induce cosmological evolution of the fundamental constants of nature?, *Phys. Rev. Lett.* **115**, 201301 (2015).
- [14] P. Sikivie, Invisible axion search methods, *Rev. Mod. Phys.* **93**, 015004 (2021).
- [15] B. M. Brubaker, L. Zhong, Y. V. Gurevich, S. B. Cahn, S. K. Lamoreaux, M. Simanovskaia, J. R. Root, S. M. Lewis, S. Al Kenany, K. M. Backes *et al.*, First results from a microwave cavity axion search at 24  $\mu\text{eV}$ , *Phys. Rev. Lett.* **118**, 061302 (2017).
- [16] K. M. Backes, D. A. Palken, S. A. Kenany, B. M. Brubaker, S. Cahn, A. Droster, G. C. Hilton, S. Ghosh, H. Jackson, S. K. Lamoreaux *et al.*, A quantum enhanced search for dark matter axions, *Nature (London)* **590**, 238 (2021).
- [17] N. Du, N. Force, R. Khatiwada, E. Lentz, R. Ottens, L. J. Rosenberg, G. Rybka, G. Carosi, N. Woollett, D. Bowring *et al.* (ADMX Collaboration), Search for invisible axion dark matter with the axion dark matter experiment, *Phys. Rev. Lett.* **120**, 151301 (2018).
- [18] C. Bartram, T. Braine, E. Burns, R. Cervantes, N. Crisosto, N. Du, H. Korandla, G. Leum, P. Mohapatra, T. Nitta *et al.* (ADMX Collaboration), Search for invisible axion dark matter in the 3.3–4.2  $\mu\text{eV}$  mass range, *Phys. Rev. Lett.* **127**, 261803 (2021).
- [19] D. J. Marsh, Axion cosmology, *Phys. Rep.* **643**, 1 (2016).
- [20] T. A. Wagner, S. Schlamminger, J. Gundlach, and E. G. Adelberger, Torsion-balance tests of the weak equivalence principle, *Classical Quantum Gravity* **29**, 184002 (2012).
- [21] A. Hees, O. Minazzoli, E. Savalle, Y. V. Stadnik, and P. Wolf, Violation of the equivalence principle from light scalar dark matter, *Phys. Rev. D* **98**, 064051 (2018).
- [22] A. Arvanitaki, S. Dimopoulos, and K. Van Tilburg, Sound of dark matter: Searching for light scalars with resonant-mass detectors, *Phys. Rev. Lett.* **116**, 031102 (2016).
- [23] S. M. Vermeulen, P. Relton, H. Grote, V. Raymond, C. Affeldt, F. Bergamin, A. Bisht, M. Brinkmann, K. Danzmann, S. Doravari *et al.*, Direct limits for scalar field dark matter from a gravitational-wave detector, *Nature (London)* **600**, 424 (2021).
- [24] R. Abbott, T. D. Abbott, F. Acernese, K. Ackley, C. Adams, N. Adhikari, R. X. Adhikari, V. B. Adya, C. Affeldt, D. Agarwal *et al.* (LIGO Scientific Collaboration, Virgo Collaboration, and KAGRA Collaboration), Constraints on dark photon dark matter using data from LIGO's and Virgo's third observing run, *Phys. Rev. D* **105**, 063030 (2022).
- [25] P. R. Saulson, Thermal noise in mechanical experiments, *Phys. Rev. D* **42**, 2437 (1990).
- [26] A. Branca, M. Bonaldi, M. Cerdonio, L. Conti, P. Falferi, F. Marin, R. Mezzena, A. Ortolan, G. A. Prodi, L. Taffarello, G. Vedovato, A. Vinante, S. Vitale, and J.-P. Zendri, Search for an ultralight scalar dark matter candidate with the AURIGA detector, *Phys. Rev. Lett.* **118**, 021302 (2017).
- [27] A. A. Geraci, C. Bradley, D. Gao, J. Weinstein, and A. Derevianko, Searching for ultralight dark matter with optical cavities, *Phys. Rev. Lett.* **123**, 031304 (2019).
- [28] J. Manley, D. J. Wilson, R. Stump, D. Grin, and S. Singh, Searching for scalar dark matter with compact mechanical resonators, *Phys. Rev. Lett.* **124**, 151301 (2020).
- [29] J. Manley, M. D. Chowdhury, D. Grin, S. Singh, and D. J. Wilson, Searching for vector dark matter with an optomechanical accelerometer, *Phys. Rev. Lett.* **126**, 061301 (2021).
- [30] M. Aspelmeyer, T. J. Kippenberg, and F. Marquardt, Cavity optomechanics, *Rev. Mod. Phys.* **86**, 1391 (2014).
- [31] C. G. Baker, W. P. Bowen, P. Cox, M. J. Dolan, M. Goryachev, and G. Harris, Optomechanical dark matter direct detection, [arXiv:2306.09726](https://arxiv.org/abs/2306.09726).
- [32] G. Afek, D. Carney, and D. C. Moore, Coherent scattering of low mass dark matter from optically trapped sensors, *Phys. Rev. Lett.* **128**, 101301 (2022).
- [33] A. J. Brady, X. Chen, K. Xiao, Y. Xia, J. Manley, M. D. Chowdhury, Z. Liu, R. Harnik, D. J. Wilson, Z. Zhang, and Q. Zhuang, Entanglement-enhanced optomechanical sensor array for dark matter searches, *Commun. Phys.* **6**, 237 (2023).
- [34] C. Murgui, Y. Wang, and K. M. Zurek, Axion detection with optomechanical cavities, [arXiv:2211.08432](https://arxiv.org/abs/2211.08432).
- [35] R. E. Lanou, H. J. Maris, and G. M. Seidel, Detection of solar neutrinos in superfluid helium, *Phys. Rev. Lett.* **58**, 2498 (1987).
- [36] W. Guo and D. N. McKinsey, Concept for a dark matter detector using liquid helium-4, *Phys. Rev. D* **87**, 115001 (2013).
- [37] K. Schutz and K. M. Zurek, Detectability of light dark matter with superfluid helium, *Phys. Rev. Lett.* **117**, 121302 (2016).
- [38] Y. You, J. Smolinsky, W. Xue, K. Matchev, T. Saab, K. Gunther, and Y. Lee, Signatures and detection prospects for sub-GeV dark matter with superfluid helium, *J. High Energy Phys.* **07** (2023) 009.

- [39] S. A. Lyon, K. Castoria, E. Kleinbaum, Z. Qin, A. Persaud, T. Schenkel, and K. M. Zurek, Single phonon detection for dark matter via quantum evaporation and sensing of  $^3\text{He}$ , *Phys. Rev. D* **109**, 023010 (2024).
- [40] H. J. Maris, G. M. Seidel, and D. Stein, Dark matter detection using helium evaporation and field ionization, *Phys. Rev. Lett.* **119**, 181303 (2017).
- [41] S. A. Hertel, A. Biekert, J. Lin, V. Velan, and D. N. McKinsey, Direct detection of sub-GeV dark matter using a superfluid  $^4\text{He}$  target, *Phys. Rev. D* **100**, 092007 (2019).
- [42] R. Anthony-Petersen, A. Biekert, C. L. Chang, Y. Chang, L. Chaplinsky, A. Dushkin, C. W. Fink, M. Garcia-Sciveres, W. Guo, S. A. Hertel *et al.*, Applying superfluid helium to light dark matter searches: Demonstration of the HeRALD detector concept, [arXiv:2307.11877](https://arxiv.org/abs/2307.11877).
- [43] B. von Krosigk, K. Eitel, C. Enss, T. Ferber, L. Gastaldo, F. Kahlhoefer, S. Kempf, M. Klute, S. Lindemann, M. Schumann *et al.*, DELight: A direct search experiment for light dark matter with superfluid helium, *SciPost Phys. Proc.* **12**, 016 (2023).
- [44] C. Gao, W. Halperin, Y. Kahn, M. Nguyen, J. Schütte-Engel, and J. W. Scott, Axion wind detection with the homogeneous precession domain of superfluid helium-3, *Phys. Rev. Lett.* **129**, 211801 (2022).
- [45] L. A. De Lorenzo and K. C. Schwab, Ultra-high Q acoustic resonance in superfluid  $^4\text{He}$ , *J. Low Temp. Phys.* **186**, 233 (2017).
- [46] B. M. Abraham, Y. Eckstein, J. B. Ketterson, M. Kuchnir, and P. R. Roach, Velocity of sound, density, and Grüneisen constant in liquid  $^4\text{He}$ , *Phys. Rev. A* **1**, 250 (1970).
- [47] V. Vadakkumbatt, M. Hirschel, J. Manley, T. J. Clark, S. Singh, and J. P. Davis, Prototype superfluid gravitational wave detector, *Phys. Rev. D* **104**, 082001 (2021).
- [48] C. Bartram, T. Braine, R. Cervantes, N. Crisosto, N. Du, G. Leum, L. J. Rosenberg, G. Rybka, J. Yang, D. Bowring *et al.* (ADMX Collaboration), Axion dark matter experiment: Run 1B analysis details, *Phys. Rev. D* **103**, 032002 (2021).
- [49] D. A. Palken, B. M. Brubaker, M. Malnou, S. A. Kenany, K. M. Backes, S. B. Cahn, Y. V. Gurevich, S. K. Lamoreaux, S. M. Lewis, R. H. Maruyama *et al.*, Improved analysis framework for axion dark matter searches, *Phys. Rev. D* **101**, 123011 (2020).
- [50] L. Krauss, J. Moody, F. Wilczek, and D. E. Morris, Calculations for cosmic axion detection, *Phys. Rev. Lett.* **55**, 1797 (1985).
- [51] H. Hirakawa, Dispersion of gravitational waves, *J. Phys. Soc. Jpn.* **35**, 295 (1973).
- [52] A. Vinante, R. Mezzena, G. A. Prodi, S. Vitale, M. Cerdonio, M. Bonaldi, and P. Falferi, Thermal noise in a high Q ultracryogenic resonator, *Rev. Sci. Instrum.* **76** (2005).
- [53] C. A. Regal, J. D. Teufel, and K. W. Lehnert, Measuring nanomechanical motion with a microwave cavity interferometer, *Nat. Phys.* **4**, 555 (2008).
- [54] M. Yuan, V. Singh, Y. M. Blanter, and G. A. Steele, Large cooperativity and microkelvin cooling with a three-dimensional optomechanical cavity, *Nat. Commun.* **6**, 8491 (2015).
- [55] D. Cattiaux, I. Golokolenov, S. Kumar, M. Sillanpää, L. Mercier de Lépinay, R. R. Gazizulin, X. Zhou, A. D. Armour, O. Bourgeois, A. Fefferman *et al.*, A macroscopic object passively cooled into its quantum ground state of motion beyond single-mode cooling, *Nat. Commun.* **12**, 6182 (2021).
- [56] D. Budker, P. W. Graham, M. Ledbetter, S. Rajendran, and A. O. Sushkov, Proposal for a cosmic axion spin precession experiment (CASPER), *Phys. Rev. X* **4**, 021030 (2014).
- [57] H. J. Paik, Superconducting tunable-diaphragm transducer for sensitive acceleration measurements, *J. Appl. Phys.* **47**, 1168 (1976).
- [58] T. J. Clark, V. Vadakkumbatt, F. Souris, H. Ramp, and J. P. Davis, Cryogenic microwave filter cavity with a tunability greater than 5 GHz, *Rev. Sci. Instrum.* **89**, 114704 (2018).
- [59] C. A. Potts and J. P. Davis, Strong magnon-photon coupling within a tunable cryogenic microwave cavity, *Appl. Phys. Lett.* **116**, 263503 (2020).
- [60] M. de Wit, G. Welker, K. Heeck, F. M. Buters, H. J. Eerkens, G. Koning, H. van der Meer, D. Bouwmeester, and T. H. Oosterkamp, Vibration isolation with high thermal conductance for a cryogen-free dilution refrigerator, *Rev. Sci. Instrum.* **90**, 015112 (2019).
- [61] M. Bignotto, M. Bonaldi, M. Cerdonio, L. Conti, F. Penasa, G. A. Prodi, G. Soranzo, L. Taffarello, and J. P. Zendri, New suspension system for the gravitational wave bar detector AURIGA, *Rev. Sci. Instrum.* **76**, 084502 (2005).
- [62] R. J. Donnelly and C. F. Barenghi, The observed properties of liquid helium at the saturated vapor pressure, *J. Phys. Chem. Ref. Data* **27**, 1217 (1998).
- [63] B. M. Abraham, Y. Eckstein, J. B. Ketterson, M. Kuchnir, and J. Vignos, Sound propagation in liquid  $^4\text{He}$ , *Phys. Rev.* **181**, 347 (1969).
- [64] B. D. Hauer, C. Doolin, K. S. D. Beach, and J. P. Davis, A general procedure for thermomechanical calibration of nano/micro-mechanical resonators, *Ann. Phys. (Amsterdam)* **339**, 181 (2013).
- [65] A. A. Clerk, M. H. Devoret, S. M. Girvin, F. Marquardt, and R. J. Schoelkopf, Introduction to quantum noise, measurement, and amplification, *Rev. Mod. Phys.* **82**, 1155 (2010).
- [66] A. Schliesser, O. Arcizet, R. Rivière, G. Anetsberger, and T. J. Kippenberg, Resolved-sideband cooling and position measurement of a micromechanical oscillator close to the Heisenberg uncertainty limit, *Nat. Phys.* **5**, 509 (2009).
- [67] L. A. De Lorenzo, Optomechanics with superfluid helium-4, Ph.D. thesis, California Institute of Technology, 2016, <https://thesis.library.caltech.edu/9781/>.
- [68] A. Vinante, Present performance and future upgrades of the AURIGA capacitive readout, *Classical Quantum Gravity* **23**, S103 (2006).
- [69] M. Cerdonio, M. Bonaldi, D. Carlesso, E. Cavallini, S. Caruso, A. Colombo, P. Falferi, G. Fontana, P. Fortini, R. Mezzena *et al.*, The ultracryogenic gravitational-wave detector AURIGA, *Classical Quantum Gravity* **14**, 1491 (1997).
- [70] M. I. Hollister, D. A. Bauer, R. C. Dhuley, P. Lukens, L. D. Martin, M. K. Ruschman, R. L. Schmitt, and G. L. Tatkowski, The cryogenics design of the SuperCDMS SNOLAB experiment, *IOP Conf. Ser.* **278**, 012118 (2017).